11th World Congress on Computational Mechanics (WCCM XI)
5th European Conference on Computational Mechanics (ECCM V)
6th European Conference on Computational Fluid Dynamics (ECFD VI)
E. Oñate, J. Oliver and A. Huerta (Eds)

ACCELERATION OF STRONGLY COUPLED FLUID-STRUCTURE INTERACTION WITH MANIFOLD MAPPING

DAVID S. BLOM*, ALEXANDER H. VAN ZUIJLEN* and HESTER BIJL*

* Faculty of Aerospace Engineering
Delft University of Technology
P. O. Box 5058, 2600 GB Delft, The Netherlands
e-mail: d.s.blom@tudelft.nl, web page: http://www.tudelft.nl/

Key words: Fluid-Structure Interaction, Manifold Mapping, Partitioned, Strong Coupling

Abstract. Strongly coupled partitioned fluid-structure interaction problems require multiple coupling iterations per time step. The fluid domain and the structure domain are solved multiple times in each time step such that the kinematic and dynamic interface conditions on the fluid-structure interface are satisfied. Quasi-Newton methods have been successfully applied in case the fluid and structure solvers are considered as black boxes, i.e. only input and output information of the solvers are used by the coupling techniques.

In this contribution a computationally inexpensive low-fidelity model is combined with a high-fidelity model in order to accelerate the convergence of the high-fidelity model. This is achieved by applying the manifold mapping algorithm on the fluid-structure interaction problem in order to minimize the fluid-structure interface residual. Originating from multi-fidelity optimization, the manifold mapping algorithm is applied for the first time in a simulation context, instead of an optimization context.

The manifold mapping algorithm is applied on a standard fluid-structure interaction benchmark, namely the cylinder flap FSI3 case. A reduction of 48 % in terms of high fidelity iterations is achieved compared with the inverse least squares Quasi-Newton algorithm, resulting in a 42 % decrease in computational costs.

1 INTRODUCTION

Fluid-structure interaction solvers are multi-physics solvers which allow to simulate dynamic responses and instabilities of complex problems. Examples of its application are aero-elasticity, arterial flow and airbag deployment [2, 9]. Also, the deployment of parachute systems can be modelled with strongly coupled fluid-structure interaction solvers. Concluding, fluid-structure interaction plays a crucial role in many engineering fields where efficient and accurate simulations are highly important.

The focus of this contribution is the numerical simulation of strongly coupled fluid-structure interaction problems, where the fluid solver and the structure solver are considered as black boxes. An implication of using only input and output information of the fluid and structural solver is that a large number of sub-iterations are necessary to obtain a strongly coupled solution. This means that both the fluid and structure solver are called multiple times per time step. One idea is to perform a large amount of the sub-iterations with a low fidelity model, instead of the current high fidelity flow and structure models [8]. The questions remains how to efficiently couple the multi-fidelity models.

Originating from multi-fidelity optimization, the aggressive space mapping algorithm has been used in [8] to efficiently couple a high fidelity model with a low fidelity model for a fluid-structure interaction problem. Scholcz et al. [8] consider the fluid-structure interaction interface problem as an optimization problem. A computationally inexpensive low-fidelity model is combined with a high-fidelity model in order to accelerate the convergence of the high-fidelity model.

In this contribution, manifold mapping is applied for the first time to a fluid-structure interaction problem in order to decrease the number of sub-iterations of the high-fidelity fluid-structure interaction model. One advantage of manifold mapping over space mapping, is that the algorithm has provable convergence to the correct solution [5]. This proof has not been shown for space mapping.

The paper is structured as follows: first, the fluid-structure interaction problem is described in section 2. Section 3 introduces the manifold mapping algorithm, and the application of the technique is shown in section 5 for a standard fluid-structure interaction benchmark, namely the cylinder with an attached flap test case [10]. The paper is finalized with the conclusions in section 6.

2 FLUID-STRUCTURE INTERACTION

The fluid-structure interaction problem is partitioned into a fluid domain Ω^f and a structural domain Ω^s. The separate domains are coupled on the fluid-structure interface $\Gamma^{f\,s}$ through the interface conditions consisting of the kinematic and dynamic boundary conditions. The governing equations for the flow and the structure are introduced in this section, and the used boundary conditions are shortly discussed.

2.1 Fluid domain

The fluid is considered to be incompressible. Hence, the governing equations for the fluid are given by the balance of momentum

$$\varrho^f \frac{\partial \boldsymbol{v}^f}{\partial t} + \varrho^f \left(\nabla \boldsymbol{v}^f\right) \boldsymbol{v}^f = \nabla \cdot \boldsymbol{\sigma}^f, \tag{1}$$

and the balance of mass, which reduces to a divergence free constraint on the velocity field due to incompressibility:

$$\nabla \cdot \boldsymbol{v}^f = 0 \qquad \text{in } \Omega^f, \tag{2}$$

where the velocity field is denoted by $\boldsymbol{v}^f$, the pressure field is denoted by p^f, and ϱ^f represents the density. A Newtonian fluid is considered, which leads to the constitutive equation for the stress tensor $\boldsymbol{\sigma}^f$

$$\boldsymbol{\sigma}^f = -p^f \boldsymbol{I} + \varrho^f \nu^f \left(\nabla \boldsymbol{v}^f + \nabla \boldsymbol{v}^{f\,T} \right), \tag{3}$$

for a given kinematic viscosity ν^f.

2.2 Structure domain

The configuration of the structure domain is described by the displacement $\boldsymbol{u}^s$. An elastic and incompressible structure is assumed, and the governing equation is given by the balance of momentum

$$\varrho^s \frac{\partial \boldsymbol{v}^s}{\partial t} + \varrho^s \left(\nabla \boldsymbol{v}^s \right) \boldsymbol{v}^s = \nabla \cdot \boldsymbol{\sigma}^s + \varrho^s \boldsymbol{g} \qquad \text{in } \Omega^s. \tag{4}$$

Equation (4) is modified to use the Lagrangian description, i.e. with respect to the initial reference state Γ^s, resulting in

$$\varrho^s \frac{\partial^2 \boldsymbol{u}^s}{\partial t^2} = \nabla \cdot \left(J \boldsymbol{\sigma}^s \boldsymbol{F}^{-T} \right) + \varrho^s \boldsymbol{g} \qquad \text{in } \Omega^s, \tag{5}$$

where the deformation gradient tensor $\boldsymbol{F}$ is defined as $\boldsymbol{F} = \boldsymbol{I} + \nabla \boldsymbol{u}^s$, and the Jacobian J is the determinant of the deformation gradient tensor $\boldsymbol{F}$. By applying the constitutive law for the St. Venant-Kirchhoff material, the Cauchy stress tensor $\boldsymbol{\sigma}^s$ is found by applying

$$\boldsymbol{\sigma}^s = \frac{1}{J} \boldsymbol{F} \left(\lambda^s \left(\operatorname{tr} \boldsymbol{E} \right) \boldsymbol{I} + 2\mu^s \boldsymbol{E} \right) \boldsymbol{F}^T, \tag{6}$$

with $\boldsymbol{E} = \frac{1}{2} \left(\boldsymbol{F}^T \boldsymbol{F} - \boldsymbol{I} \right)$, and the shear modulus is denoted by μ^s.

2.3 Interface conditions

At the fluid-structure interface $\Gamma^{f\,s}$, the balance of stresses is enforced through

$$\boldsymbol{\sigma}^f \boldsymbol{n} = \boldsymbol{\sigma}^s \boldsymbol{n} \qquad \text{on } \Gamma^{f\,s}, \tag{7}$$

with the unit vector $\boldsymbol{n}$ normal to the fluid-structure interface $\Gamma^{f\,s}$. Also, the no-slip condition is imposed so that velocities must be equal at the fluid-structure interface:

$$\boldsymbol{v}^f = \boldsymbol{v}^s \qquad \text{on } \Gamma^{f\,s}. \tag{8}$$

2.4 Partitioned coupling as interface optimization

The fluid solver and structure solver are considered as black boxes. In other words, only the input and output information is accessible. Therefore, the response of the fluid solver F is defined as

$$\boldsymbol{y} = F(\boldsymbol{x}), \tag{9}$$

where $\boldsymbol{x}$ denotes the velocity of the fluid-structure interface, i.e. $\boldsymbol{x} = \boldsymbol{v}^f = \boldsymbol{v}^s$, and $\boldsymbol{y}$ denotes the force acting on the fluid-structure interface defined as $\boldsymbol{y} = \boldsymbol{\sigma}^f \boldsymbol{n}$. The response of the structure solver S is consequently defined as

$$\boldsymbol{x} = S(\boldsymbol{y}). \tag{10}$$

Typically, at every time step the fixed point equation

$$\boldsymbol{x} = S \circ F(\boldsymbol{x}) \tag{11}$$

must be satisfied, which can also be written as the interface residual $\boldsymbol{R}(\boldsymbol{x})$

$$\boldsymbol{R}(\boldsymbol{x}) = S \circ F(\boldsymbol{x}) - \boldsymbol{x}, \tag{12}$$

which is solved with a minimization or optimization procedure aimed to find the optimal solution $\boldsymbol{x}^\star$ such that

$$\boldsymbol{x}^\star = \arg\min_{\boldsymbol{x}} ||\boldsymbol{R}(\boldsymbol{x})||_2. \tag{13}$$

Standard approaches used to solve the strongly coupled fluid-structure interaction problem are the Gauss-Seidel method, fixed under-relaxation, Aitken under-relaxation, and the IQN-ILS method [2]. These minimization procedures require the evaluation of $S \circ F(\boldsymbol{x})$ multiple times per time step.

Algorithms originally developed for multi-fidelity optimization, such as aggressive space mapping and output space mapping [1], can also be used to minimize the interface residual $\boldsymbol{R}(\boldsymbol{x})$ [8]. Where Scholcz et al. [8] apply a space mapping algorithm to the interface residual problem $\boldsymbol{R}(\boldsymbol{x}) = S \circ F(\boldsymbol{x}) - \boldsymbol{x}$, this contribution investigates the use of manifold mapping [5] in order to solve this optimization problem.

3 MANIFOLD MAPPING

Manifold mapping is a surrogate-based optimization technique, which means that the quality of the initial solution or approximation is iteratively improved. The main aim of a surrogate-based optimization technique, is to decrease the computational times of high fidelity models by combining the high fidelity model with a less accurate and computationally less expensive coarse model.

The main advantage of the manifold mapping algorithm is that it has provable convergence to the correct solution contrary to aggressive space mapping or output space

mapping [5]. This makes the algorithm more robust for use in a fluid-structure interaction simulation.

The basic terminology is introduced, and the manifold mapping algorithm is shown. For convergence theorems for the different manifold mapping algorithms available, the reader is referred to [5].

3.1 Manifold mapping terminology

Two types of models are distinguished: a fine model and a coarse model. The fine model response is denoted by $\boldsymbol{f} : X \subset \mathbb{R}^n \rightarrow \mathbb{R}^m$, where $\boldsymbol{x} \in X$ represents the control variable of the optimization problem. It is assumed that the fine model is accurate, but requires high computational costs to evaluate.

3.1.1 Fine model

The fine model cost function is defined as $F(\boldsymbol{x}) = ||\boldsymbol{f}(\boldsymbol{x}) - \boldsymbol{q}||$, which represents the discrepancy between the design specification $\boldsymbol{q}$ and a particular response of the model $\boldsymbol{f}(\boldsymbol{x})$. Thus, the following minimization problem should be solved:

$$\boldsymbol{x}_f{}^{\star} = \arg\min_{\boldsymbol{x} \in X} ||\boldsymbol{f}(\boldsymbol{x}) - \boldsymbol{q}||. \tag{14}$$

When the manifold mapping technique is applied to the fluid-structure interaction problem, the fine model response is defined as the interface residual:

$$\boldsymbol{f}(\boldsymbol{x}) = \boldsymbol{R}(\boldsymbol{x}) = S \circ F(\boldsymbol{x}) - \boldsymbol{x}. \tag{15}$$

The design specification $\boldsymbol{q}$ is the zero vector. For consistency, $\boldsymbol{q}$ is not dropped from the formulation, since the design specification of the coarse model is not zero, but iteratively updated. This is discussed next.

3.1.2 Coarse model

The coarse model response is denoted by $\boldsymbol{c} : Z \subset \mathbb{R}^n \rightarrow \mathbb{R}^m$, where $\boldsymbol{z} \in Z$ represents the control variable of the coarse model. In the general case, an additional mapping $\overline{\boldsymbol{p}} : X \rightarrow Z$ is introduced, such that the space mapping function

$$\boldsymbol{p}(\boldsymbol{x}) = \arg\min_{\boldsymbol{z} \in Z} ||\boldsymbol{c}(\boldsymbol{z}) - \boldsymbol{f}(\boldsymbol{x})|| \tag{16}$$

is minimized in order to minimize the misalignment between the coarse model and the fine model [4]. The coarse model response is defined as $\boldsymbol{c}(\boldsymbol{z}) = \tilde{S} \circ \tilde{F}(\boldsymbol{z}) - \boldsymbol{z}$.

In this work, it is assumed that the space mapping function is close to identity which is a common assumption also applied in [4]. The optimization procedure is performed on the so-called coupling grid, as proposed in [3]. The coarse model response $\boldsymbol{c}$ is interpolated

with radial basis functions to the coupling grid at every coarse model iteration, and the control variable $\boldsymbol{z}$ is also interpolated with radial basis functions from the coupling grid to the coarse model.

The coarse model cost function is defined as

$$\boldsymbol{z}^{\star} = \arg\min_{\boldsymbol{z}\in Z} ||\boldsymbol{c}(\boldsymbol{z}) - \boldsymbol{q}|| \,. \tag{17}$$

The Euclidean norm or L_2 norm is used in the minimization process.

3.2 Manifold mapping algorithm

The manifold mapping $\boldsymbol{S} : \boldsymbol{c}(Z) \rightarrow \boldsymbol{f}(X)$ is introduced with the goal to correct for the misalignment between the fine and coarse model. $\boldsymbol{S}$ is defined as the affine mapping

$$\boldsymbol{S}\,\boldsymbol{c}(\boldsymbol{x}) = \boldsymbol{f}({\boldsymbol{x}_f}^{\star}) + \overline{S}\,(\boldsymbol{c}(\boldsymbol{x}) - \boldsymbol{c}({\boldsymbol{x}_f}^{\star}))\,, \tag{18}$$

for an unknown solution ${\boldsymbol{x}_f}^{\star}$ and with $\overline{S}$ specified as

$$\overline{S} = J_{\boldsymbol{f}}({\boldsymbol{x}_f}^{\star})\, {J_{\boldsymbol{c}}}^{\dagger}({\boldsymbol{x}_f}^{\star})\,, \tag{19}$$

and the pseudoinverse is indicated with the symbol †. The Jacobian of the fine model evaluated at ${\boldsymbol{x}_f}^{\star}$ is denoted with $J_{\boldsymbol{f}}({\boldsymbol{x}_{\boldsymbol{f}}}^{\star})$, and the Jacobian of the coarse model evaluated at ${\boldsymbol{x}_f}^{\star}$ is denoted with $J_{\boldsymbol{c}}({\boldsymbol{x}_{\boldsymbol{f}}}^{\star})$.

In [5] it is shown that

$$\boldsymbol{x}_{\boldsymbol{f}}^{\star} = \arg\min_{\boldsymbol{x}\in X} ||\boldsymbol{S}\,\boldsymbol{c}(\boldsymbol{x}) - \boldsymbol{q}|| = \arg\min_{\boldsymbol{x}\in X} \left|\left|\boldsymbol{c}(\boldsymbol{x}) - \boldsymbol{c}({\boldsymbol{x}_{\boldsymbol{f}}}^{\star}) + \overline{S}^{\dagger}\,(\boldsymbol{f}({\boldsymbol{x}_{\boldsymbol{f}}}^{\star}) - \boldsymbol{q})\right|\right|, \tag{20}$$

which is the basis of the manifold mapping algorithm. The mapping $\boldsymbol{S}$ is not known at forehand, and is therefore iteratively approximated.

Thus, the manifold mapping algorithm generates a sequence of mappings $\boldsymbol{S}_k, k \geq 0$, and consists of the following steps:

1. Set $k = 0$ and initialize the manifold mapping algorithm with an initial guess $\boldsymbol{x}_0$. Here, the initial guess at time level $u+1$ is determined by extrapolating the solutions of the previous time steps: ${\boldsymbol{x}_{\boldsymbol{0}}}^{u+1} = \frac{5}{2}\boldsymbol{x}^{u} - 2\boldsymbol{x}^{u-1} + \frac{1}{2}\boldsymbol{x}^{u-2}$. This is different from the original manifold mapping algorithm, which determines $\boldsymbol{x}_0$ with the coarse model optimum $\boldsymbol{x}_0 = \arg\min_{\boldsymbol{z}\in Z} ||\boldsymbol{c}(\boldsymbol{z})||$.

2. Initialize the mapping matrix S_k of size $m \times m$ as the identity matrix.

3. Evaluate $\boldsymbol{f}(\boldsymbol{x}_k)$ and $\boldsymbol{c}(\boldsymbol{x}_k)$, and go to the next time step in case the convergence criteria are met, i.e. when the fixed point equation $\boldsymbol{x}_k = S \circ F(\boldsymbol{x}_k)$ is satisfied for the fine model.

$\boldsymbol{x_0}^{u+1} = \frac{5}{2}\boldsymbol{x}^u - 2\boldsymbol{x}^{u-1} + \frac{1}{2}\boldsymbol{x}^{u-2}$
$S_0 = I_{m\times m}$
for $k = 0 \rightarrow k_{max}$ **do**
  $\boldsymbol{q}_k = \boldsymbol{c}(\boldsymbol{x}_k) - S_k(\boldsymbol{f}(\boldsymbol{x}_k) - \boldsymbol{q})$
  $\boldsymbol{x}_{k+1} = \arg\min_{\boldsymbol{x}\in X} ||\boldsymbol{c}(\boldsymbol{x}) - \boldsymbol{q}_k||$
  $\Delta F = \left[\boldsymbol{f}(\boldsymbol{x}_{k+1}) - \boldsymbol{f}(\boldsymbol{x}_k), \cdots, \boldsymbol{f}(\boldsymbol{x}_{k+1}) - \boldsymbol{f}\left(\boldsymbol{x}_{\max(k+1-n,0)}\right)\right]$
  $\Delta C = \left[\boldsymbol{c}(\boldsymbol{x}_{k+1}) - \boldsymbol{c}(\boldsymbol{x}_k), \cdots, \boldsymbol{c}(\boldsymbol{x}_{k+1}) - \boldsymbol{c}\left(\boldsymbol{x}_{\max(k+1-n,0)}\right)\right]$
  $(U_f, \Sigma_f, V_f) = SVD(\Delta F)$
  $(U_c, \Sigma_c, V_c) = SVD(\Delta C)$
  $\Delta F^\dagger = V_f {\Sigma_f}^\dagger {U_f}^T$
  $S_{k+1} = \Delta C\, \Delta F^\dagger + I_{m\times m} - U_c {U_c}^T$
end for

Figure 1: The manifold mapping (MM) algorithm

4. For $k > 0$, define $\Delta F = \left[\boldsymbol{f}(\boldsymbol{x}_{k+1}) - \boldsymbol{f}(\boldsymbol{x}_k), \cdots, \boldsymbol{f}(\boldsymbol{x}_{k+1}) - \boldsymbol{f}\left(\boldsymbol{x}_{\max(k+1-n,0)}\right)\right]$ and $\Delta C = \left[\boldsymbol{c}(\boldsymbol{x}_{k+1}) - \boldsymbol{c}(\boldsymbol{x}_k), \cdots, \boldsymbol{c}(\boldsymbol{x}_{k+1}) - \boldsymbol{c}\left(\boldsymbol{x}_{\max(k+1-n,0)}\right)\right]$. Their singular value decompositions are determined as $\Delta C = U_c \Sigma_c {V_c}^T$ and $\Delta F = U_f \Sigma_f {V_f}^T$. The pseudoinverse of ΔF is evaluated as $\Delta F^\dagger = U_f {\Sigma_f}^\dagger {V_f}^T$.

5. Update the mapping S_k with $S_{k+1} = \Delta C\, \Delta F^\dagger + I_{m\times m} - U_c {U_c}^T$.

6. The solution $\boldsymbol{x}_k$ is updated with $\boldsymbol{x}_k = \arg\min_{\boldsymbol{x}\in X} ||\boldsymbol{c}(\boldsymbol{x}) - \boldsymbol{c}(\boldsymbol{x}_k) + S_k(\boldsymbol{f}(\boldsymbol{x}_k) - \boldsymbol{q})||$.

7. Set $k := k + 1$ and go to step 3.

The algorithm is also shown in figure 1.

3.3 Convergence criteria

For the fine model a relative convergence criteria is used, i.e. the iteration is assumed to be converged if the relative residual ϵ_f is smaller than a certain specified tolerance TOL_f:

$$\epsilon_f = \frac{||\, S \circ F(\boldsymbol{x}) - \boldsymbol{x}\,||}{||\boldsymbol{x}||} \leq TOL_f. \tag{21}$$

For the coarse model the following criteria is used:

$$\epsilon_c = \frac{||\, \tilde{S} \circ \tilde{F}(\boldsymbol{z}) - \boldsymbol{z} - \boldsymbol{q}\,||}{||\boldsymbol{z} - \boldsymbol{q}||} \leq TOL_c. \tag{22}$$

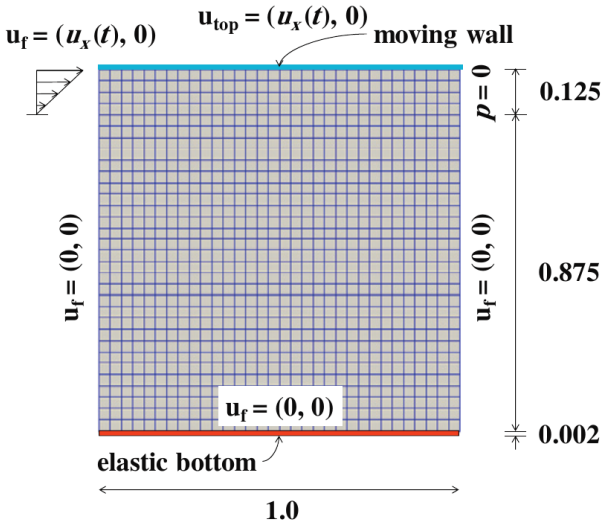

Figure 2: Overview of the lid-driven cavity tests. The boundary conditions and the geometry is shown. The dimensions are shown in meters. The figure has been taken from [6].

4 RESULTS FOR THE LID-DRIVEN CAVITY CASE WITH A FLEXIBLE BOTTOM

As a first test case, a lid-driven cavity with a flexible bottom is considered. The benchmark consists of a two-dimensional laminar flow in a square cavity with a flexible bottom membrane. The case has been used in [6] to validate a strongly coupled fluid-structure interaction solver. Here, the benchmark is used to compare the performance of the manifold mapping algorithm with the standard IQN-ILS algorithm, and with two space mapping techniques, namely aggressive space mapping (ASM) and output space mapping (OSM).

At the top wall and at the inlet an oscillating boundary condition is applied given by

$$u_x(t) = 1 - \cos\left(\frac{2\pi}{5}t\right). \tag{23}$$

At the inlet the horizontal velocity depends linearly on the vertical coordinate, as shown in figure 2. For further details regarding this case, the reader is referred to [6]. The test case is simulated until $t = 5\,s$ with time step $\Delta t = 0.01\,s$. The structure elasticity parameter has the value $\varrho_f/\varrho_s = 1/50$.

The mesh of the fine model consist of 65 536 cells for the fluid domain and 2 048 cells for the structure domain. The fluid mesh of the fine model is coarsened twice in x and y direction, resulting in 4 096 cells for the fluid domain. The structure mesh of the coarse model consists of 2 048 cells. The fine model uses a matching mesh at the fluid-structure interface, whereas the coarse model uses a non-matching mesh at the fluid-structure interface. The coupling iterations are assumed to be converged in case $\epsilon_f \leq 10^{-4}$. For the coarse model, the tolerance setting $TOL_c = 10^{-4}$ is used.

Table 1: Average number of fine and coarse iterations per time step for the lid-driven cavity case with a flexible bottom. The iteration numbers are averaged over the complete simulation. The iteration numbers are shown for the manifold mapping technique, aggressive space mapping, output space mapping, and the standard interface quasi-Newton inverse least squares method only operating on the fine mesh.

	# fine eval.	**# coarse eval.**	**duration [min]**
MM	4.3	11.1	3.5
ASM-ILS	52.3	63.9	34.8
OSM	4.9	11.7	6.1
IQN-ILS	7.0	0.0	6.0

Table 1 shows the number of fine model and coarse model evaluations for the complete simulation. The manifold mapping algorithm is compared with aggressive space mapping (ASM-ILS), output space mapping (OSM), and the current state-of-the-art coupling algorithm IQN-ILS. As shown in the table, the manifold mapping uses the least amount of fine and coarse evaluations compared to the other coupling algorithms, and requires 1.6 times less fine model evaluations compared to IQN-ILS.

The aggressive space mapping algorithm shows a large number of iterations per time step. This is due to the fact that convergence of the space mapping algorithm is not guaranteed, and for some time steps the coupling algorithm does not converge and stalls. The manifold mapping approach does not have this problem.

5 RESULTS FOR THE CYLINDER WITH AN ATTACHED FLAP BENCHMARK

The fluid-structure interaction benchmark introduced in [10] describes a two-dimensional incompressible laminar flow around a fixed cylinder with an attached flexible cantilever. The geometry of the test case is shown in figure 3. A parabolic inlet boundary condition is prescribed, and a free outflow boundary condition is applied at the right boundary.

In [10] three different test cases are considered which differ in the material and flow parameters. This contribution only considers the FSI3 case, where the structure elasticity parameter is set to $\varrho_F/\varrho_S = 1$ resulting in a strong coupling between the fluid and the structure.

The mesh of the fine model consist of 95 696 cells for the fluid domain and 1 312 cells for the structure domain. The mesh of the fine model is coarsened twice in x and y direction, resulting in 5 981 cells for the fluid domain and 82 cells for the structure domain. Thus the ratio of the number of cells between the fine model and the coarse model is 16. Both the fine model and the coarse model apply a matching mesh at the fluid-structure interface.

Table 2 shows the results for the cylinder with an attached flap benchmark comparing the manifold mapping with aggressive space mapping, output space mapping, and the standard interface quasi-Newton inverse least-squares method. The manifold mapping

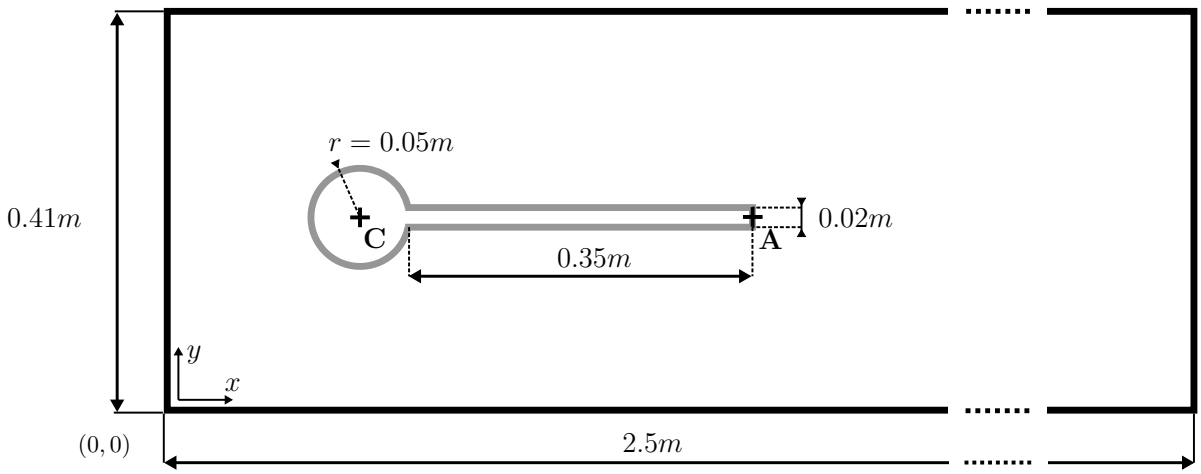

Figure 3: Geometry of the cylinder with an attached flap benchmark originally proposed in [10]. The figure shows a channel flow with a fixed cylinder and a flexible flap attached to the cylinder. Point A located at the back of the flap is used as a reference point for the measurements of the displacement. The figure has been taken from [7].

methods needs the least amount of fine model and coarse model evaluations, and requires 1.8 times less fine model evaluations compared to IQN-ILS.

Aggressive space mapping requires the largest amount of fine model and coarse model evaluations. The large number of coarse model evaluations can be explained by the fact that the aggressive space mapping algorithm requires the optimization of the coarse model to find $\boldsymbol{z}^\star$, whereas this is not required for output space mapping and manifold mapping. The simulations show that the prediction step used by the MM and OSM techniques results in a smaller initial residual compared to ASM-ILS, which results in an increase of fine model evaluations. Also, convergence of the space mapping algorithm has not been proven, and for some time steps the aggressive space mapping algorithm does not converge.

6 CONCLUSIONS

A new coupling algorithm for the efficient simulation of fluid-structure interaction is developed by using the manifold mapping (MM) technique. A computationally inexpensive low-fidelity model is combined with a high-fidelity model in order to accelerate the convergence of the coupling procedure of the high-fidelity model.

A reduction of a factor two in terms of high fidelity iterations is achieved compared with the inverse least squares Quasi-Newton algorithm, resulting in a speedup of 1.7. Future research will cover (1) a study on reuse of input/output information from previous time steps in order to further accelerate the convergence of the manifold mapping algorithm, and (2) a parallel coupling procedure such that the displacement of the fluid-structure

Table 2: Average number of fine and coarse iterations per time step for the cylinder with an attached flexible flap benchmark. The iteration numbers are averaged over the complete simulation. The iteration numbers are shown for the manifold mapping technique, aggressive space mapping, output space mapping, and the standard interface quasi-Newton inverse least squares method only operating on the fine mesh.

	# fine eval.	**# coarse eval.**	**duration [min]**
MM	6.1	29.5	12.4
ASM-ILS	21.7	65.5	32.0
OSM	7.2	31.3	13.2
IQN-ILS	11.8	0.0	21.3

interface and the forces acting on the interface are both used by the coupling algorithm.

REFERENCES

[1] Bandler, J. W., et al. Space mapping: the state of the art. *IEEE Transactions on microwave theory and techniques*, **52**(1):337–361 (2004).

[2] Degroote, J. Partitioned Simulation of Fluid-Structure Interaction. *Archives of Computational Methods in Engineering*, **20**(3):185–238 (2013). ISSN 1134-3060.

[3] Degroote, J. and Vierendeels, J. Multi-level quasi-Newton coupling algorithms for the partitioned simulation of fluid-structure interaction. *Computational Methods in Applied Mechanics and Engineering*, **225-228**:14–27 (2012).

[4] Echeverría, D. and Hemker, P. W. Space mapping and defect correction. *Computational Methods in Applied Mathematics*, **5**(2):107–136 (2005).

[5] Echeverría, D. and Hemker, P. W. Manifold mapping: a two-level optimization technique. *Computing and Visualization in Science*, **11**(4-6):193–206 (2008). ISSN 1432-9360. doi:10.1007/s00791-008-0096-y.

[6] Habchi, C., et al. Partitioned Solver for strongly coupled fluid-structure interaction. *Computers & Fluids*, **71**:306–319 (2013).

[7] Mehl, M., et al. Parallel coupling numerics for partitioned fluid-structure interaction simulations. *SIAM Scientific Computing* (submitted 2013).

[8] Scholcz, T. P., et al. Accelerated partitioned fluid-structure interaction using space-mapping. In *Proceedings of 10th World Congress on Computational Mechanics* (2012).

[9] Stein, K., et al. Parachute fluid-structure interactions: 3-D computation. *Computational Methods in Applied Mechanics and Engineering*, **190**(3-4):373–386 (2000).

[10] Turek, S. and Hron, J. Proposal for Numerical Benchmarking of Fluid-Structure Interaction between an Elastic Object and Laminar Incompressible Flow. In Bungartz, H.-J. and Schäfer, M., editors, *Fluid-Structure Interaction*, volume 53 of *Modelling, Simulation, Optimisation*, pages 371–385. Springer Berlin Heidelberg (2006).